PHYSICAL REVIEW B **94**, 205101 (2016)

Multiple charge density wave states at the surface of $TbTe_3$

Ling Fu,[1] Aaron M. Kraft,[1] Bishnu Sharma,[1] Manoj Singh,[1] Philip Walmsley,[2,3] Ian R. Fisher,[2,3] and Michael C. Boyer[1,*]
[1]*Department of Physics, Clark University, Worcester, Massachusetts 01610, USA*
[2]*Geballe Laboratory for Advanced Materials and Department of Applied Physics, Stanford University, Stanford, California 94305-4045, USA*
[3]*Stanford Institute for Materials and Energy Sciences, SLAC National Accelerator Laboratory, 2575 Sand Hill Road, Menlo Park, California 94025, USA*

(Received 25 July 2016; revised manuscript received 30 September 2016; published 1 November 2016)

We studied $TbTe_3$ using scanning tunneling microscopy (STM) in the temperature range of 298–355 K. Our measurements detect a unidirectional charge density wave (CDW) state in the surface Te layer with a wave vector consistent with that of the bulk $\boldsymbol{q}_{\mathrm{CDW}} = 0.30 \pm 0.01\boldsymbol{c}^*$. However, unlike previous STM measurements, and differing from measurements probing the bulk, we detect two perpendicular orientations for the unidirectional CDW with no directional preference for the in-plane crystal axes (a or c axis) and no noticeable difference in wave vector magnitude. In addition, we find regions in which the bidirectional CDW states coexist. We propose that observation of two unidirectional CDW states indicates a decoupling of the surface Te layer from the rare-earth block layer below, and that strain variations in the Te surface layer drive the local CDW direction to the specific unidirectional or, in rare occurrences, bidirectional CDW orders observed. This indicates that similar driving mechanisms for CDW formation in the bulk, where anisotropic lattice strain energy is important, are at play at the surface. Furthermore, the wave vectors for the bidirectional order we observe differ from those theoretically predicted for checkerboard order competing with stripe order in a Fermi-surface nesting scenario, suggesting that factors beyond Fermi-surface nesting drive CDW order in $TbTe_3$. Finally, our temperature-dependent measurements provide evidence for localized CDW formation above the bulk transition temperature T_{CDW}.

DOI: 10.1103/PhysRevB.94.205101

I. INTRODUCTION

Charge density wave (CDW) states are broken-symmetry states prevalent in condensed matter systems, where they are often found to coexist and/or compete with other orders. In particular, in the intensely studied graphene-related systems [1], layered chalcogenides [2,3], organic compounds [4], cuprate high-temperature superconductors [5–9], and BiS_2 superconductors [10], CDW states are observed to coexist with superconductivity. However, the specifics of how CDWs interact with other orders, on the nanoscale, are far from understood. Furthermore, even a fundamental understanding of CDW states and their origin remains incomplete.

While CDW states in some materials are believed to be understood within the more traditional theoretical framework of electronic instabilities driven by Fermi-surface nesting [11–14], often referred to as a Peierls instability, recent experimental and theoretical work shows that CDW states in other material systems are not understood within this framework. Instead, the properties of CDW states in these systems, including members of the transition-metal dichalcogenide family, are determined by strongly momentum-dependent electron-phonon coupling [15–19]. Developing an understanding of CDW states and their origins is critical to gaining insight into complex systems where a CDW state may be only one of several orders present.

The rare-earth tritellurides ($R\mathrm{Te}_3$ where R = rare-earth ion) are compounds where the understanding of the driving mechanism for CDW states has evolved. The $R\mathrm{Te}_3$ compounds are quasi-two-dimensional materials which have an alternating structure of neighboring conducting square Te planes (double Te planes) separated by insulating rare-earth block layers, as seen in Fig. 1(a). Below T_{CDW}, a bulk unidirectional incommensurate CDW state is established primarily within the Te planes along the c crystal axis with $\boldsymbol{q}_{\mathrm{CDW}} \sim (2/7)\boldsymbol{c}^*$ [20–23]. The $R\mathrm{Te}_3$ compounds with heavier rare-earth ions (R = Dy, Ho, Er, Tm, and Tb) undergo a second CDW transition at lower temperatures where a CDW state along the a axis, $\boldsymbol{q}_{\mathrm{CDW2}} \sim (1/3)\boldsymbol{a}^*$, is established coexisting with the c axis CDW [24,25].

Angle-resolved photoemission spectroscopy (ARPES) measurements coupled with electronic structure calculations show that the Fermi surface of the $R\mathrm{Te}_3$ compounds have significant parallel sheets, favoring Fermi-surface nesting-driven CDWs in these materials [23,26–28]. Owing to a slight orthorhombicity in the crystal structure, with the a axis smaller than the c axis (e.g. $a \approx 4.312$ Å and $c \approx 4.314$ Å for $TbTe_3$ near the bulk T_{CDW}) [24], the unidirectional CDW preferentially forms along the c axis at the higher-temperature CDW transition. However, it has been noted that there is only a moderate enhancement in the real and imaginary components of the Lindhard susceptibility at $\boldsymbol{q} = 0.25\boldsymbol{c}^*$ which is close to, but differs slightly from, the experimentally measured CDW wave vector of $\boldsymbol{q}_{\mathrm{CDW}} = 0.30\boldsymbol{c}^*$, leading to questions as to whether Fermi-surface nesting alone can fully account for the observed CDW in these compounds [16,29]. Recent inelastic x-ray scattering measurements on $TbTe_3$ find that, at T_{CDW}, there is evidence for both a renormalization of the soft phonon mode toward zero energy and a peak in the linewidth for the soft phonon mode centered at $\boldsymbol{q} = 0.3\boldsymbol{c}^*$, consistent with the experimentally observed CDW wave vector [29]. In turn, these x-ray measurements, as well as Raman spectroscopy

---

[*] Author to whom correspondence should be addressed: mboyer@clarku.edu

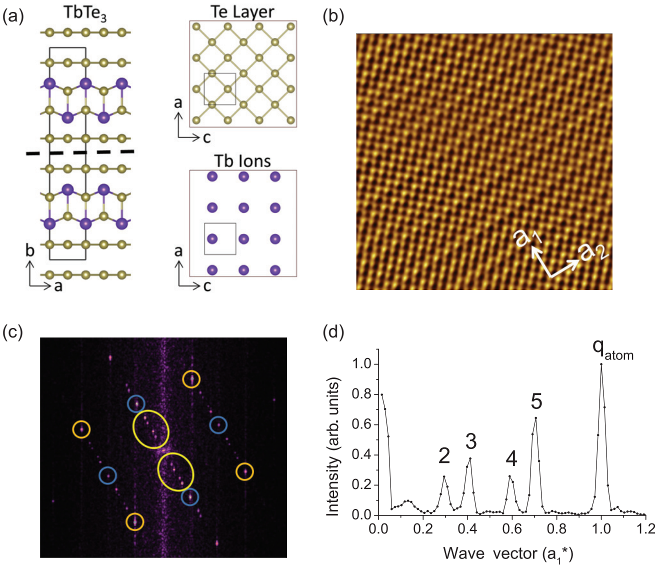

FIG. 1. (a) At left, the crystal structure for $TbTe_3$ with a black rectangle outlining the unit cell. The dotted line indicates the *a-c* cleave plane between the double Te layers. At right, the square lattice of the Te layer which is exposed by cleaving as well as the locations of the closest Tb ions in the rare-earth block layer directly below. The unit cell is again shown in the structures at right for reference. The crystal structures were constructed using Vesta software [51]. (b) Topographic image taken over a 90 Å square region at $I = 65\,\text{pA}$, $V_{\text{Sample}} = -350\,\text{mV}$. The Te square lattice of the exposed surface can be clearly seen as well as superimposed "stripes" associated with a unidirectional CDW state along the a_1 crystal axis. We use a_1 and a_2 to denote the in-plane crystal axes for our measurements since we observe unidirectional CDW order along both axes. This prevents us from unambiguously identifying the *a* and *c* crystal axes. (c) FFT of a typical topographic image. Orange circles identify the wave vectors associated with Te square lattice. Blue circles identify the wave vectors associated with the subsurface rare-earth block layer (Tb ions). The yellow ovals enclose peaks in the FFT which are associated with the unidirectional CDW as well as those arising from mixing between the CDW wave vector and block atomic wave vectors. (d) Line cut through the FFT, beginning at the origin (center), in the direction of the CDW (through yellow oval), and ending just past $\boldsymbol{q}_{\text{atom}}$ (blue circle) associated with the block layer.

measurements conducted on $ErTe_3$ [30], suggest momentum-dependent electron-phonon coupling plays an important role in the formation of CDW states in the RTe_3 compounds. While a full understanding of the driving mechanism for CDW states in the RTe_3 compounds is still incomplete, it appears that both Fermi-surface instabilities and momentum-dependent electron-phonon coupling may play a role [31].

In this paper, we present results of temperature-dependent (298–355 K) scanning tunneling microscopy (STM) studies on $TbTe_3$, which has a bulk $T_{\text{CDW}} \sim 336\,\text{K}$ below which a unidirectional CDW is established along the *c* axis. In our measurements, we surprisingly detect spatially separated unidirectional CDW states along both the *a* and *c* crystal axes as well as regions where the perpendicular CDW states coexist. We propose that the multiple CDW orders established at the surface of $TbTe_3$ are driven by a strain field induced in a weakly coupled Te surface layer through sample cleaving. Using bias-dependent measurements, we investigate the application of the one-dimensional Peierls model to CDW states in $TbTe_3$. In addition, through temperature-dependent measurements, we find evidence for local CDW order above bulk T_{CDW}.

II. EXPERIMENTAL METHODS

$TbTe_3$ single crystals were grown using a self-flux technique described in detail elsewhere [32]. Our studies were conducted using an RHK PanScan STM operating in an ultrahigh vacuum (UHV) chamber with a base pressure $\sim 5 \times 10^{-10}$ Torr in a temperature range of 298–355 K. Atomically resolved STM tips were prepared by chemical etching of tungsten wire, followed by *in situ* conditioning-annealing, followed by fine sharpening through electron bombardment. The $TbTe_3$ samples studied were cleaved in UHV by mechanically striking a cleave bar epoxied to the sample surface. Previous STM measurements [33,34] show that RTe_3 compounds cleave between the double Te planes such that the STM tip directly probes the exposed Te surface.

III. RESULTS

A. Unidirectional CDW states

Figure 1(b) shows a topographic image of the surface of $TbTe_3$ acquired at 298 K. The exposed square Te lattice (often referred to as a Te square net) is observed. Superimposed upon the square lattice are parallel "stripes" due to an established unidirectional CDW state. The fast Fourier transform (FFT) of a typical topographic image [Fig. 1(c)] shows three major components. First, there are four peaks (orange circles) due to the square Te surface layer with nearest neighbor spacing ∼3 Å. Second, rotated 45°, are four peaks (blue circles) associated with a square lattice originating from the rare-earth block layer below. Density functional theory electronic-structure calculations indicate that the block layer current signal detected by STM is dominated by the rare-earth ion [34], in our case Tb with nearest neighbor Tb spacing of ∼4.3 Å. Third, the peaks in the FFT enclosed by yellow ovals are due to the presence of the unidirectional CDW state.

The observation of a unidirectional CDW in $TbTe_3$ for temperatures just below T_{CDW} is typically a good indicator of the *c* axis of the crystal, given that a long-range CDW is established along the *c* axis in the bulk. However, at different regions across the sample surface, and for the same crystal cleave, our measurements show extended regions (400 Å or larger) containing a unidirectional CDW in either of two perpendicular orientations. Furthermore, there is no general preference for the direction of the observed unidirectional CDW; it is equally likely that the CDW will be observed in either of the two directions. The establishment of unidirectional CDWs along two perpendicular crystal axes prevents us from unambiguously identifying the *a* and *c* crystal axes from our STM measurements. For this reason, in describing the CDW in our measurements, we often refer to the crystal axes in the *a-c* crystal plane as a_1 and a_2 instead of the traditional *a*- and *c*-axis designation. We find the CDW wave vectors along the two crystal axes are equivalent in magnitude to within the typical resolution of our FFTs: $\boldsymbol{q}_1 = (0.30 \pm 0.01)\boldsymbol{a}_1^*$ and

$\boldsymbol{q}_2 = (0.30 \pm 0.01)\boldsymbol{a}_2^*$. In the bulk, $a_1{}^*$ and $a_2{}^*$ differ by only $\sim 0.002\,\text{Å}^{-1}$ at 300 K according to x-ray measurements [24].

Such an observation of unidirectional CDWs along both the a and c crystal axes is very surprising given the purely c axis unidirectional CDW in the bulk. Bulk crystals can harbor stacking faults, corresponding to a 90° crystal misorientation during crystal growth, which could possibly account for the observation (i.e. successive cleaves of the same crystal could possibly reveal 90° rotation of the a and c axes). Based on individual STM measurements, one cannot rule out such a scenario, although we note that x-ray measurements indicate, at minimum, that the vast majority of the sample is in a single orientation, whereas we observe perpendicular orientations of the unidirectional CDWs on multiple samples and sample cleaves with no general preferential direction to the observed orientation. Significantly, however, we observe regions of the sample where the two unidirectional CDWs coexist, providing compelling evidence that unidirectional CDWs can indeed exist at the surface in both a and c directions. Furthermore, as we will discuss in greater detail in subsequent sections of this paper, these regions evolve continuously from a-axis oriented, to simultaneous order, to c-axis oriented CDWs upon translating across the surface of the sample, without encountering any step edges. Our measurements clearly indicate a relaxation at the surface of bulk constraints which would otherwise favor formation of the unidirectional CDW along the c axis over the a axis. This suggests that the surface Te layer is only weakly coupled to the bulk below, a possibility on which we will expand in more detail in the Discussion section.

B. Wave vector mixing and tip-condition effects

Figure 1(d) shows a line cut through the FFT of the topography [Fig. 1(c)] in the direction of the CDW, starting at the origin, passing through the four peaks enclosed in yellow, and ending at $\boldsymbol{q}_{\text{atom}}$, the peak associated with the block layer circled in blue. In addition to $\boldsymbol{q}_{\text{atom}}$, we label the four peaks as 2, 3, 4, and 5, representing peaks at $\sim 2/7, \sim 3/7, \sim 4/7$, and $\sim 5/7 q_{\text{atom}}$, respectively. These multiple peaks have been previously explained as originating from wave vector mixing of the true CDW signal with the atomic (Tb) block layer signal as well as mixing of their harmonics [33,34]. More specifically, wave vector mixing arises due to the asymmetric coupling between two sinusoidal signals. Given that the tunneling current has contributions from the top Te layer, in which the CDW state predominantly resides, as well as from the rare-earth block layer below, it is not surprising that these signals may become coupled through measurement setup conditions. As a consequence of this coupling, there arises a contribution to the total signal which resembles the product of two sinusoidal functions. Using standard trigonometric identities, this product can be re-expressed as the sum of two sinusoidal functions with periodicities given by the sum and difference of the original wave vectors.

While the STM studies of TbTe_3 by Fang *et al.* [33] and of the related CeTe_3 by Tomic *et al.* [34] observe the same four peaks in FFTs of topographic images, the two studies assumed differing fundamental CDW wave vectors and consequently different wave vector mixing scenarios to explain the origin of the multiple peaks.

Fang *et al.* presents the following peak origins:
Peak 2 : $q_{\text{atom}} - q_{\text{CDW}}$; Peak 3 : $2q_{\text{CDW}} - q_{\text{atom}}$; Peak 4 : $2q_{\text{atom}} - 2q_{\text{CDW}}$; Peak 5 : q_{CDW}.

Tomic *et al.* provides an alternative:
Peak 2 : q_{CDW}; Peak 3 : $q_{\text{atom}} - 2q_{\text{CDW}}$; Peak 4 : $2q_{\text{CDW}}$; Peak 5 : $q_{\text{atom}} - q_{\text{CDW}}$.

The "true" CDW wave vectors identified in each scenario are equivalent up to a reciprocal lattice vector, so scattering measurements cannot distinguish between the two wave vector possibilities. However, if the wave vector mixing peaks arise as artifacts, purely due to measurement setup conditions as previously suggested [33–35], it should be possible to identify the true CDW wave vector. In particular, peak 4 in Tomic's wave-vector-mixing scenario is purely the first harmonic of $\boldsymbol{q}_{\text{CDW}}$. On the other hand, peak 4 in Fang's wave-vector-mixing scenario results from the mixing of two signals: (1) the first harmonic of the atomic signal and (2) the first harmonic of the CDW signal. If one were to remove the first harmonic of the atomic signal, then any wave-vector-mixing peaks resulting from coupling to this true signal will also necessarily be removed. Specifically, if one were to remove the first harmonic atomic signal, and peak 4 remains, then peak 4 cannot be due to wave vector mixing.

It is possible to effectively do this by examining data where the tip is in a "good" but not "great" condition. In other words, the tip is good enough that, when acquiring a topography, we can identify the CDW, Te lattice, and rare-earth block layer peaks in the FFT. However, the tip is not great in that the harmonics of the atomic signals are not present (e.g. are indistinguishable from the noise level). The bottom plot in Fig. 2(a) illustrates this situation where the first harmonic of the block peak ($2q_{\text{atom}}$) is clearly missing. However, all of the CDW and mixing peaks, including peak 4, are present as they are in the middle and top plots when the block harmonic signal is present. As a result, we conclude that the true CDW wave vector is $\boldsymbol{q}_{\text{CDW}} \sim 2/7\boldsymbol{c}^*$, not $\sim 5/7\boldsymbol{c}^*$. Consistent with this, the peak near ~ 1.3 in the bottom plot is present as expected for $\boldsymbol{q}_{\text{CDW}} \sim 2/7\boldsymbol{c}^*$, since this peak represents $q_{\text{atom}} + q_{\text{CDW}}$. However, the peak at ~ 1.4 is at the noise level, consistent with it disappearing. Since the ~ 1.4 peak results from $2q_{\text{atom}} - 2q_{\text{CDW}}$, its disappearance is to be expected when the harmonic signal $2q_{\text{atom}}$ is absent.

We emphasize that distinguishing between the two possible CDW wave-vector-mixing scenarios in the above fashion relies on the assumption that the wave-vector-mixing peaks originate purely from STM measurement setup conditions. However, it is well established that there is a physical coupling of the Te planes to the neighboring block layers in the $R\text{Te}_3$ compounds [36,37]. Therefore, if the wave-vector-mixing peaks originate not from STM setup conditions as previously suggested, but rather from a physical coupling of the CDW to the block layer, then distinguishing between the two scenarios based on FFT peak differences, or lack thereof (arising from the presence or absence of the atomic harmonic signal in STM data), is not possible. However, if wave-vector-mixing peaks arise due to a physical coupling, this could potentially open the door to future investigations using STM to understand and characterize CDW coupling to the block layer.

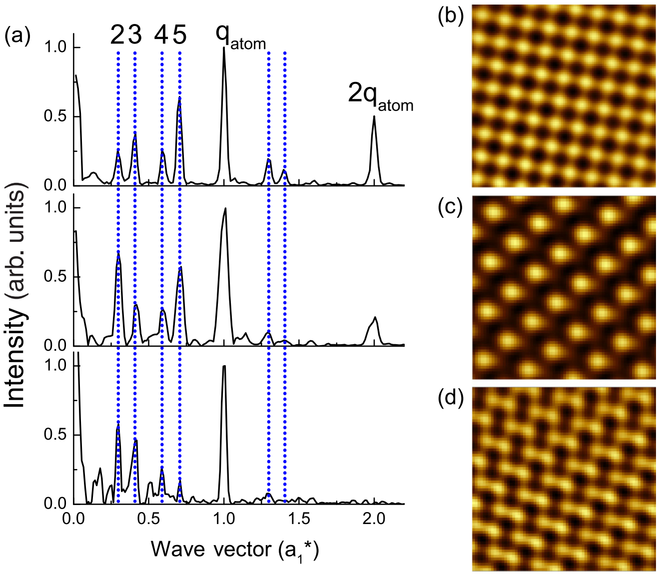

FIG. 2. (a) Line cuts through FFTs in the direction of the CDW [as in Fig. 1(d) but now extending past $2q_{\text{atom}}$]. The harmonic of the block signal $2q_{\text{atom}}$ is present in the top and middle plots, but absent in the bottom plot. Peak 4 is present in all three cases, indicating that peak is not the result of wave vector mixing involving the block harmonic, as the harmonic is absent in the bottom plot, but peak 4 is still present. Slightly different tip conditions lead to variations in the relative intensities of the peaks in the FFT. Each of the FFTs, from which the line cuts are extracted, were taken on 400 Å square topographic images acquired with the same settings: $I = 50\,\text{pA}$ and $V_{\text{sample}} = +150\,\text{mV}$ with the same number of pixels and at temperatures at least 10 K below the bulk T_{CDW}. (b)–(d) 25 Å square topographies which have been Fourier filtered to include only contributions from the Te net and rare-earth block signals. Small differences in tip conditions lead to (b) a Te-dominated topography, (c) a rare-earth block-dominated topography, and (d) a topography which has the appearance of surface dimerization.

We note that Fang *et al.* determined $\boldsymbol{q}_{\text{CDW}} \sim 5/7\boldsymbol{c}^*$ based on their bias-dependent measurements [33]. Namely, at higher biases, they found the $\sim 2/7\boldsymbol{c}^*$ peak intensity diminished very significantly, whereas the $\sim 5/7\boldsymbol{c}^*$ peak was noticeably prominent. We do not observe any such peak-intensity bias dependence in our measurements. Rather, we find that the peak intensities of the CDW and mixing peaks are dependent on the tip condition. As an example, Fig. 2(a) shows that, in one case (at top), the $\sim 2/7\boldsymbol{c}^*$ peak is weaker than the $\sim 5/7\boldsymbol{c}^*$, whereas in the middle and bottom plots, the $\sim 2/7$ peak is stronger for measurements at the same bias.

Furthermore, Fig. 2(a) illustrates that the relative peak intensities in the FFT, and consequently features observed in topographic images [Figs. 2(b)–2(d)], are sensitive to slight differences in the tip condition. For certain tip conditions (the most typical case), the Te square surface net is most prominent in our images [Fig. 2(b)]. In other images, the rare-earth block layer is more prominent [Fig. 2(c)]. Furthermore, we have acquired topographic images where the tip condition is such that the sum of the Te and block signals produces a topography which has the appearance of dimerization [Fig. 2(d)], a feature noted by Fang *et al.* [33]. If we Fourier filter individual Te or block-layer peaks for the topography in Fig. 2(d), we see only the expected Te square lattice and the block square lattice, respectively. However, when we filter to include both the Te and block peaks, we see the appearance of dimerization. We believe the previously identified dimerization is due, in part, to a tip effect linked to the relative tunneling current components originating from the Te surface layer and the rare-earth block layer below and is not evidence of a true surface dimerization. We provide more details regarding this dimerization appearance in the Discussion section.

Since we have highlighted the effects due to slight changes in the tip condition, it is worthwhile to emphasize what does and does not change with tip condition. While the relative intensity of peaks in the FFT are linked to tip condition, and hence the topographical features which might be immediately apparent visually, the CDW, wave vector mixing, and lattice wave vectors associated with the peaks do not change. As a result, other than exploiting the tip condition to aid in distinguishing between a 2/7 and 5/7 CDW wave vector, we emphasize that the results detailed in this paper are independent of tip condition.

C. Bias-dependent measurements

While the $R\text{Te}_3$ compounds were initially believed to be prototypical Fermi-surface nesting-driven CDW compounds, more recent studies indicate the importance of momentum-dependent electron-phonon coupling in the establishment of CDW states in these materials. Bias-dependent STM measurements have the potential to give insight into the origin of CDW states. Namely, in the case of a CDW state described within the one-dimensional Peierls model, the electron and hole components of the CDW are expected to be spatially out of phase [16,19,38]. Such a model has been applied to quasi-one-dimensional systems such as the blue bronzes and NbSe_3 where ARPES and band structure calculations determine that there are substantial parallel components of their Fermi surfaces [12,13,39,40]. In NbSe_3, the expected bias-dependent contrast inversion in the CDW state has been detected by STM [41] despite imperfect nesting [40]. To our knowledge, similar measurements have not been conducted on the blue bronzes.

Quasi-two-dimensional materials such as $\text{K}_{0.9}\text{Mo}_6\text{O}_{17}$ and η-Mo_4O_{11} have been shown to have a "hidden" one-dimensional nature [42–45], motivating the possibility of applying a one-dimensional Peierls model to understand CDW states in these systems. Whereas the Fermi surface of $\text{K}_{0.9}\text{Mo}_6\text{O}_{17}$ leads to "extremely good nesting" conditions [43], the Fermi surface of η-Mo_4O_{11} allows for only imperfect nesting [44]. In each case, STM has directly imaged bias-dependent contrast inversion in the CDW state, which has been used to support the case for CDW states described by the one-dimensional Peierls model arising in a two-dimensional system [46,47]. Similar to η-Mo_4O_{11}, tight-binding modeling of the Te layer in the $R\text{Te}_3$ compounds reveals a one-dimensional character to the material due to the anisotropy of the p_x and p_z orbitals within the Te plane [28]. In the idealized model, the one-dimensional chains separately formed by the p_x and p_z orbitals would lead to a near-perfect nesting-driven CDW state. However, coupling between the chains leads to an imperfect nesting scenario [48], similar to η-Mo_4O_{11}.

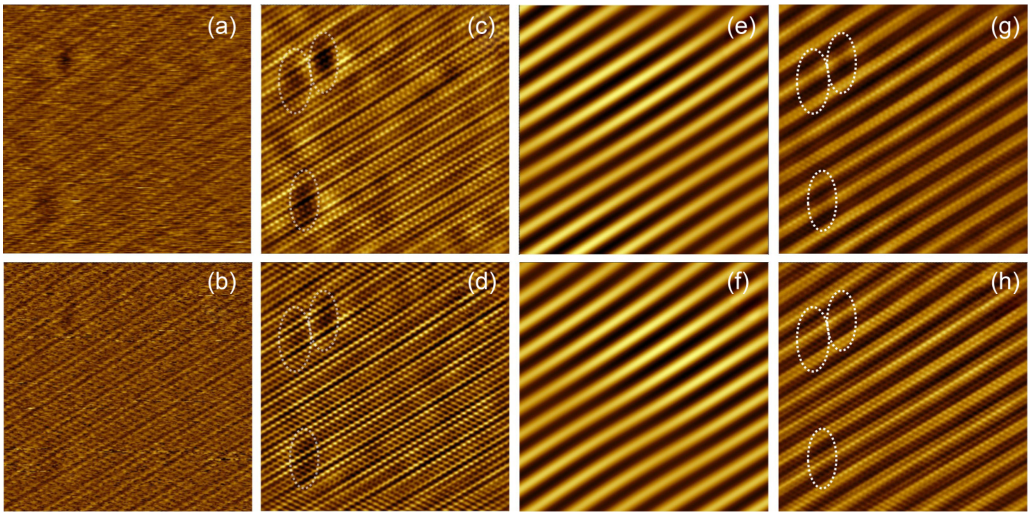

FIG. 3. (a) and (b) 154 Å square topographies taken over the exact same location with $I = 30\,\text{pA}$ and $V_{\text{Sample}} = +100\,\text{mV}$ [for (a)] and $V_{\text{Sample}} = -100\,\text{mV}$ [for (b)]. (c) and (d) Images in (a) and (b) Fourier filtered to include the Te, block, and CDW/wave-vector-mixing signals as well as low wave vector signals. The three dark regions visible in (a) and (b) are enhanced through the filtering and circled with white ovals. The white ovals extend over identical regions in the two images. (e) and (f) Using Fourier filtering, only the $\sim 2/7a_1$ CDW for $+100\,\text{mV}$ [in (e)] and $-100\,\text{mV}$ [in (f)] is shown. There is no phase shift evident in the CDW as imaged at positive or negative biases. (g) and (h) The CDW signals in (e) and (f) are enhanced by 15 times and added to the filtered image in (c) and (d), respectively, allowing for identification of the CDW maxima and minima relative to the three ovals for $+100\,\text{mV}$ [in (g)] and $-100\,\text{mV}$ [in (h)]. Using the ovals as a guide, these images clearly indicate that the CDW at positive and negative biases are in phase.

We acquired bias-dependent measurements to determine whether there is a phase shift in the CDW state imaged at positive and negative biases near the Fermi energy. Figures 3(a) and 3(b) show topographic images taken over the same 154 Å square region at +100 and −100 mV, respectively. We Fourier filtered the two images to visually enhance three common "dark spot" surface features which we have circled with white ovals [Figs. 3(c) and 3(d)]. We emphasize that the white ovals are of exactly the same size and extend over identical regions in the two images. We then Fourier filtered the images such that only the CDW contribution is included in the images [Figs. 3(e) and 3(f)]. We note that the CDW maxima and minima appear to align with each another. To examine this more closely, we enhanced the CDW signals in Figs. 3(e) and 3(f) by a factor of 15 and added it to the original filtered topographies [Figs. 3(c) and 3(d)], resulting in the images seen in Figs. 3(g) and 3(h). In the images appearing in Figs. 3(g) and 3(h), using as reference the common three white ovals, it is clear there is no phase shift between the CDW maxima and minima seen at +100 and −100 mV. In contrast to other two-dimensional CDW compounds with a one-dimensional character, we do not observe bias-dependent contrast inversion of the CDW state in our measurements. Apparently the simple one-dimensional Peierls model does not apply to TbTe_3, possibly reflecting contributions to the density of states from reconstructed (metallic) parts of the quasi-two-dimensional Fermi surface, and perhaps suggestive that factors beyond Fermi-surface nesting might play a significant role in the CDW formation.

D. Temperature dependence

While the bulk CDW transition in TbTe_3 as determined by resistivity, x-ray, specific heat, and ultrasonic measurements occurs near $T_{\text{CDW}} \sim 336\,\text{K}$ [24,49], x-ray measurements have observed superlattice peaks up to 363 K [24]. These CDW-associated superlattice peaks have been attributed to CDW fluctuations. The presence of such fluctuations indicates the possibility of localized CDW order above the bulk transition temperature. Such localized CDW order above bulk T_{CDW} has been directly visualized by STM in NbSe_2; defects act as nucleation sites from which the long-range CDW forms with decreasing temperature near T_{CDW} [18].

We conducted temperature-dependent measurements from 298 K, below the bulk T_{CDW}, to 355 K, above T_{CDW}. At all temperatures within this range (taken at $\sim 5\,\text{K}$ increments, or in $\sim 1\,\text{K}$ increments between 325 and 347 K), we have been able to detect a unidirectional CDW state. Figure 4(a) shows a 90 Å square topographic image acquired at 355 K in which a unidirectional CDW state is clearly observed. A line cut through the FFT in the direction of the CDW shows the standard four associated CDW and wave-mixing peaks [Fig. 4(b)]. In our measurements at 345 K, we find regions where CDW order is present and others where it is absent, indicating strong variations in the CDW at this temperature. Such variations are particularly obvious in our measurements at 339 K. Figures 4(c) and 4(d) show a 240 × 200 Å topographic region (raw image and Fourier filtered to enhance CDW, respectively) where there are variations in the unidirectional CDW along the a_1 axis. Specifically, the CDW state in regions in the left half of the image appears weak or even absent. To emphasize these spatial variations in the CDW state, we took an FFT of the left half of the image and separately an FFT of the right half of the image [Fig. 4(e)]. We subtracted the approximately exponential background from the line cut through the FFTs to allow for quantitative comparison of the CDW peaks. We find that the $\sim 2/7\boldsymbol{a}_1{}^*$ peak is ~ 3 times larger for the right side of the image compared to the left.

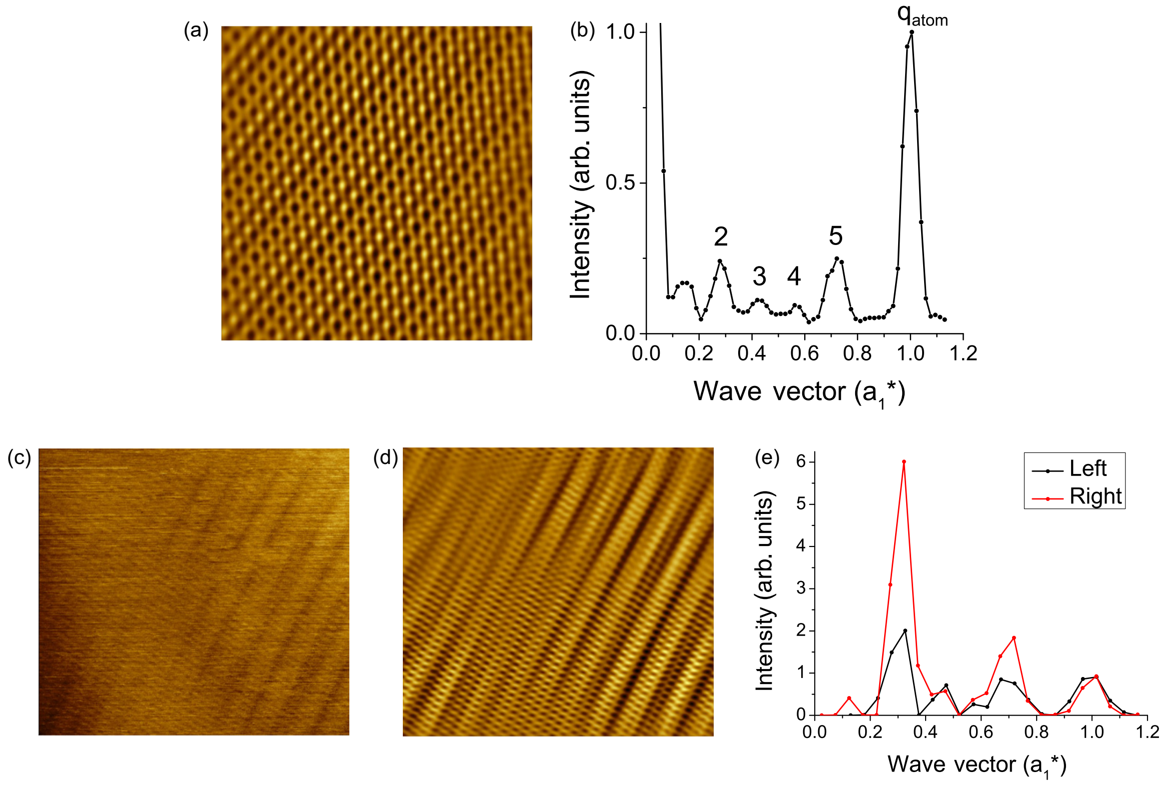

FIG. 4. (a) 90 Å square topography taken at 355 K with $V_{\text{sample}} = +200\,\text{mV}$ and $I = 40\,\text{pA}$. The image was Fourier filtered to include the surface Te lattice, block layer, and CDW/wave vector mixing signals. (b) Line cut through the FFT [of the raw topographic image for (a)] beginning at the origin, in the direction of the CDW, ending at the $\boldsymbol{q}_{\text{atom}}$ associated with the block layer. The standard 4 CDW/wave-vector-mixing peaks are observed. (c) A 240 × 200 Å topography acquired at 339 K showing variations in the unidirectional CDW state across the region with $V_{\text{sample}} = -200\,\text{mV}$ and $I = 70\,\text{pA}$. (d) The image in (c) Fourier filtered to include Te net, block layer, and CDW/wave-vector-mixing signals to visibly emphasize local variations in the CDW state. (e) A comparison of the line cuts through the FFTs separately for the left and right halves of image (c). The $\sim 2/7\boldsymbol{a}_1{}^*$ CDW peak is ∼3 larger in the right half as compared to that of the left, illustrating strong variation in the a_1-axis CDW in this region.

Our measurements detect localized CDW order and spatial variations in that order at temperatures above the bulk transition. We propose that, instead of nucleating from surface or subsurface defects, such local formation of CDW states is attributed to weak coupling of the Te layer to the bulk, coupled with strain variations across the surface layer, possibly leading to spatially varying and locally associated surface T_{CDW}s. We will provide support for this surface decoupling in the Discussion session, as well as motivate the origin of the strain variations. Finally, in our measurements, we find no temperature-dependent preferential CDW orientation (a_1 versus a_2 axis) and no temperature evolution in the magnitudes of the measured CDW wave vectors $\boldsymbol{q}_1$ and $\boldsymbol{q}_2$.

E. Coexisting CDW states

We have acquired data in which the FFT indicates the presence of CDWs along both the a_1 and a_2 axes (hence a axis and c axis) within a ∼500 Å square region [Fig. 5(a)]. Due to noise at lower wave vectors, we focus on the four wave-vector-mixing peaks around the block layer signal, $\vec{q}_{\text{atom}} \pm \vec{q}_{\text{CDW1}}$ and $\vec{q}_{\text{atom}} \pm \vec{q}_{\text{CDW2}}$, which are enclosed within a dotted yellow circle in Fig. 5(a) and are shown in detail in Fig. 5(b). The small yellow circles located at $\vec{q}_{\text{atom}} \pm \vec{q}_{\text{CDW1}}$ in Fig. 5(b) indicate the presence of a CDW along the a_1 axis and the red circles located at $\vec{q}_{\text{atom}} \pm \vec{q}_{\text{CDW2}}$ indicate the presence of a CDW along the a_2 axis.

To acquire a more local view, we broke the ∼500 Å square image into smaller regions. Figure 5(c) shows a 150 Å square image in which the CDWs along both the a_1 and a_2 axes spatially coexist. We then examined 150 Å square regions directly to the left and to the right of this "middle" region where the two CDW states coexist. The "right" region shows an a_1-axis-dominated CDW, and the "left" region shows an a_2-axis-dominated CDW [Figs. 5(d) and 5(e)]. The "middle" 150 Å region appears to not only surprisingly represent a region where two perpendicular CDW states coexist, but appears to be a transition region between regions where one of the unidirectional CDWs is more dominant. This apparently smooth transition from an a_1-axis-dominated CDW to an a_2-axis-dominated CDW region is clearly indicated by Fig. 5(f).

Such coexistence of perpendicular CDW states in TbTe_3 appears in the bulk only below ∼41 K [25]. In the bulk, the a-axis CDW has a wave vector of $\sim(1-0.68)\boldsymbol{a}^* = 0.32\boldsymbol{a}^*$, compared to the c-axis CDW wave vector of $\sim(1-0.71) = 0.29\boldsymbol{c}^*$ at 10 K [25]. The coexisting CDWs and slight differences in their wave vector magnitudes were first detected in STM measurements by Fang *et al.*, and they noted identical wave vector differences between the two CDWs. On the other hand, in our measurements conducted near room temperature,

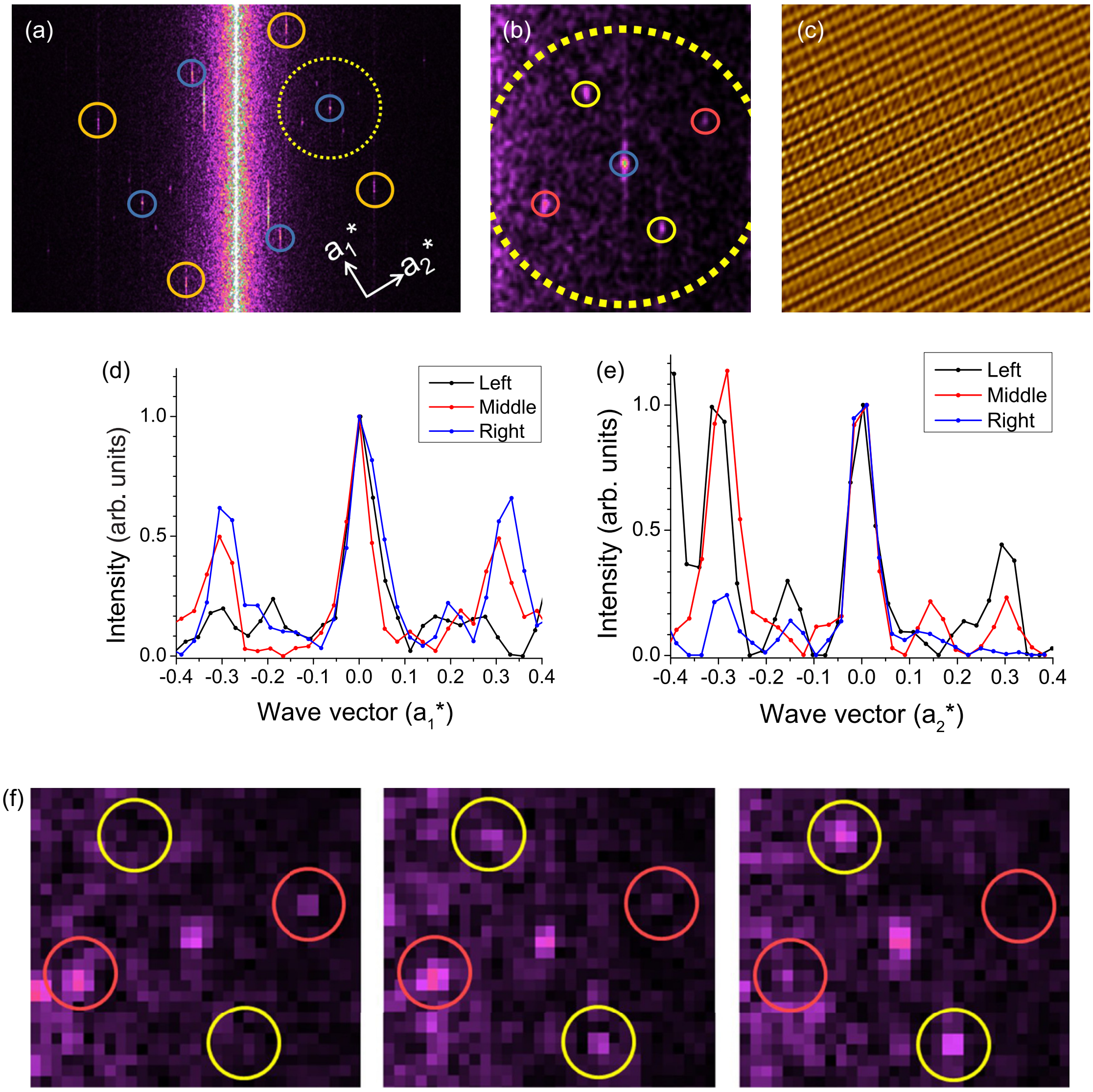

FIG. 5. (a) FFT of a ~500 Å square topography taken at 309 K with $V_{\text{sample}} = +150$ mV and $I = 50$ pA. Standard lattice peaks are circled in orange (Te net) and blue (block layer). In addition to these peaks, we observe peaks associated with two perpendicular CDWs within this field of view. Due to noise at low wave vectors, these CDW peaks are most clearly seen in the square pattern surrounding the block peak (seen within dotted yellow circle). (b) The region within the dotted yellow circled area of the FFT in (a) is enlarged to evince the block layer and CDW peaks. The peaks associated with the CDWs along the a_1 and a_2 axes are enclosed by small yellow and red circles, respectively. (c) A 150 Å square region cropped from the larger topographic image where the two CDWs spatially coexist with one another. The image was Fourier filtered to reduce noise which obscured some of the topographic features. (d) and (e) A comparison of CDW-associated peak intensities associated with the a_1-axis [in (d)] and a_2-axis [in (e)] CDWs across three neighboring 150 Å square regions (designated left, middle, right). The plots show an overlay of line cuts in either (d) the $\boldsymbol{a_1}^*$ direction or (e) $\boldsymbol{a_2}^*$ direction taken through FFTs [such as that shown in (b)] for each of the regions. For each line cut, the rare-earth block layer peak is centered at zero and the CDW-associated peaks are seen near ±0.3. There is a progression from an a_2-axis-dominated CDW at left to an a_1-axis-dominated CDW at right. (f) This progression is easily seen visually as the a_1-axis CDW peaks (in yellow) around the block signal in the FFT become more intense from left to right while the a_2-axis CDW peaks (in red) become less intense. The three FFTs are zoomed similar to what was done in (b) with the block layer signal centered, and share a common color scale.

we find $\boldsymbol{q}_{1,2} \approx 0.30\boldsymbol{a}^*_{1,2}$ (extracted from the FFT of the ~500 Å square image), which is consistent with the wave vector magnitudes when only a single unidirectional CDW is present in a given location at the surface.

It is very surprising to observe coexisting CDWs at temperatures ~7.5 times higher than the low-temperature CDW transition in TbTe$_3$. Furthermore, the wave vector magnitudes for the two coexisting CDWs are equivalent near room temperature, but have a noted difference at low temperature, even by STM. Such a difference may be accounted for by temperature-dependent differences in the coupling of surface states to the bulk. Namely, at the elevated temperatures at which we are conducting our experiments, the surface Te layer is more weakly coupled to the bulk than at lower temperatures.

Finally, we note that the spatially coexisting CDW orders we observe differ from the bidirectional checkerboard state

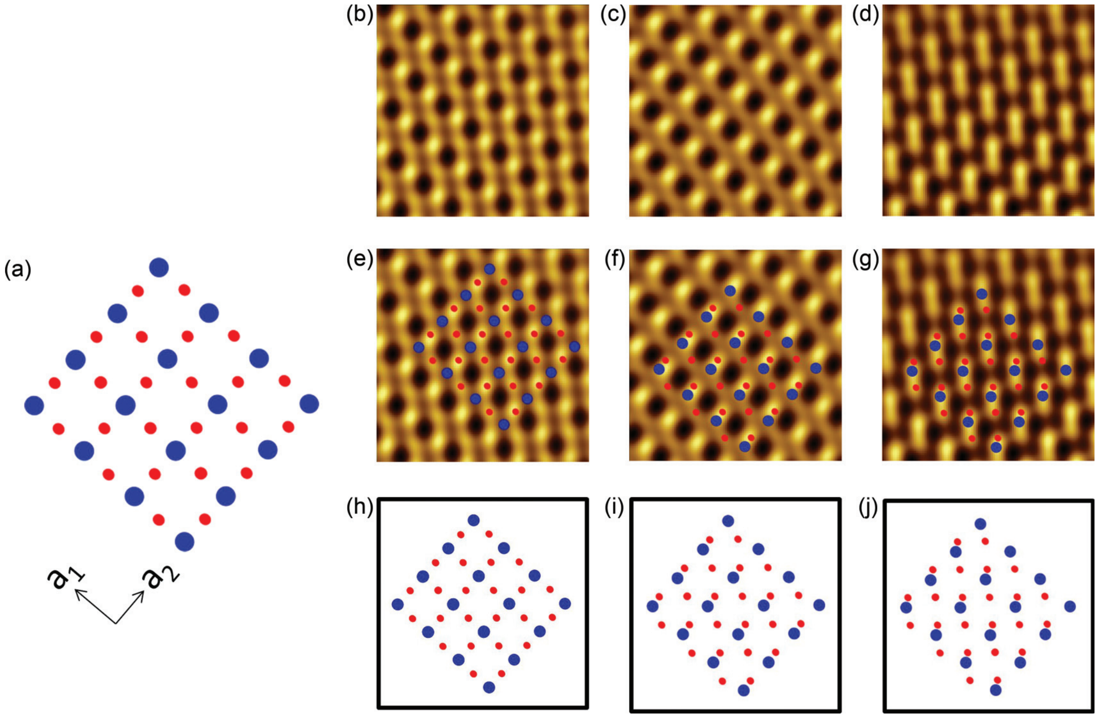

FIG. 6. (a) Relative bulk positions of Te ions (red) in the Te layer and nearest Tb ions (blue) from the rare-earth block layer directly below, projected onto the a-c plane. The axes are labeled as a_1 and a_2 since we are unable to distinguish the a and c axes in our measurements. (b)–(d) 25 Å square images cropped, respectively, from the bottom, middle, and top thirds of a Fourier filtered 120 Å square image. The Fourier filtered image only includes contributions from the Te and block-layer (Tb) structural signals. The block-layer signal was enhanced by a factor of 10 such that the Te and block-layer signals are comparable. The differing images suggest differing relative locations for the Tb and Te ions in the three regions. (e)–(g) The specific lattice positions of the Te and Tb ions superimposed on the bottom, middle, and top images. For clarity, the Te and Tb ion positions for the bottom, middle, and top images are shown separately in (h), (i), and (j), respectively. The shifts in the relative ion positions suggest a decoupling of the Te layer from the rare-earth layer below.

theoretically detailed by Yao *et al.* [28]. Yao *et al.* suggest that checkerboard order competes with unidirectional stripe CDW order in the RTe$_3$ compounds. Specifically, in their analysis, the Fermi-surface nesting vectors leading to bidirectional order are rotated relative to the individual nesting vector possibilities leading to unidirectional CDW order. In our measurements of TbTe$_3$, we find the CDW wave vectors for the bidirectional order are identical to those of the unidirectional states. This agreement points towards a nonnesting scenario driving CDW order in this material.

IV. DISCUSSION

Our STM measurements indicate differences in the CDW states at the surface compared to that of the bulk. In particular, at the surface, we observe spatially separated as well as spatially coexisting unidirectional CDWs along the both the a and c crystal axes at room temperature and above, whereas only a c-axis unidirectional CDW is detected in the bulk in this temperature range. Such differences suggest that the surface Te layer is only weakly coupled to the bulk below. To investigate whether there is evidence that the surface Te layer is decoupling from the bulk, we performed detailed analysis of topographic images to determine whether there is evidence for a shift in the Te ions from their expected lattice sites. Specifically, because the tunneling current contains a contribution from the surface Te layer and a contribution from the block layer originating from the Tb ions, it is possible to use Fourier filtering to determine the crystal structure specific to each layer as well as the relative positions of the two sets of ions. Figure 6(a) shows the bulk crystal lattice locations of the Te ions (in red) from the Te layer and nearest Tb ions (in blue) from the block layer below, the two ions which dominate the tunneling current signal, as seen projected onto the a-c plane.

We present analysis on a single ~120 Å square topographic image from which a 90 Å square appears in Fig. 1(b). We Fourier filtered the 120 Å square topographic image so as to include only the Te and block-layer lattice contributions. Because the topographic image is Te dominated, the block-layer signal was enhanced by a factor of 10 during the filtering process so that the Te and block-layer signals are of comparable size. Figures 6(b)–6(d) show three 25 Å square regions cropped from the resulting filtered image taken from within the bottom, middle, and top thirds of the image, respectively. Visually, the three images differ significantly, an indication that the Te ions may be in differing locations relative to the Tb ions in each of the three regions. Separately filtering the Te and Tb signals allows for a determination of the Te and Tb ion locations for each of the three regions. Figures 6(e)–6(g) show the locations of each ion, Te in red and Tb in blue, for each region overlaid on the 25 Å images. To further elucidate the ion locations, Figs. 6(h)–6(j) show the ion locations for the three regions. There is a progression: at the bottom of the image the Te ions are in their expected locations based on the bulk crystal structure, in the middle they are shifted noticeably, and at the top their shift is even more pronounced. These shifts cannot be explained as due to the periodic lattice distortion induced by the CDW state as the shifts seen in the middle and top regions occur predominantly along the a_2 axis, whereas the local CDW state is induced along the a_1 axis.

This analysis provides strong evidence for a decoupling of the Te surface layer from the rare-earth block layer below. Such a decoupling is not entirely surprising since it has been noted previously [21] that the Te-Te bond length in the Te layer of the bulk, which is ~3.1 Å, is considerably longer than the typical Te-Te covalent bonding length of 2.76 Å [50], leading to a structural instability. As a consequence, upon cleaving, the surface Te layer is no longer constrained from above, as it would be in the bulk, allowing the surface to relax to a more stable configuration. In addition, the cleaving process itself can induce strain variations across the weakly coupled surface layer, possibly leading to surface corrugations. As a consequence, we propose that these local strain variations affect the specifics of electron-phonon coupling in the surface Te layer, which in turn determine the axial direction of the locally established unidirectional CDW, or in rare cases, establish coexisting bidirectional order. Similar strain variations in the surface of $NbSe_2$ due to subsurface defects were proposed to drive local CDW order from tridirectional to unidirectional, whereas only the tridirectional ordering is reported in the bulk [17]. In addition, a very recent study combining x-ray and density functional theory calculations shows that anisotropic lattice strain energy plays a critical role in establishing the unidirectional CDW state along the c axis in the bulk of $TbTe_3$ [31]. The sensitivity of the CDW direction in the bulk to lattice strain illustrates how strain variations in the Te surface layer could drive the two perpendicular CDW orders observed in our measurements.

Additional analysis of the 120 Å square region is consistent with this interpretation. The lattice parameters a_1 and a_2 are the expected 4.31 ± 0.01 Å and 4.31 ± 0.03 Å, respectively, based on the Tb ion locations. Using the Te ion locations to calculate the lattice parameters, we find $a_1 = 4.28 \pm 0.37$ Å and $a_2 = 4.25 \pm 0.06$ Å. These smaller lattice-parameter averages, based on the Te ion locations, are consistent with an overall Te lattice relaxation. The larger standard deviations can be accounted for as strain-induced local lattice variations. We note that there is an expected Te lattice parameter variation of ~3% along the CDW axis due to the CDW modulation [23] corresponding to ~0.13 Å. The Te lattice variations along the CDW axis a_1 are considerably larger by about a factor of three.

Finally, our analysis also indicates the origin of the appearance of dimerization, as previously noted by Fang *et al.* [33] in their STM measurements and as seen in some of our acquired topographies such as Fig. 2(d). This dimerization, as elucidated by Fig. 6(g), is the result of two factors: (1) a shift of the Te ions from their expected location and (2) a tip condition such that the components of tunneling current originating from the Te and block layers are similar in magnitude. While this dimerization does not represent an additional true broken symmetry at the surface, it is an important indicator that the surface Te layer is decoupling from the block layer below.

V. CONCLUSION

Our studies motivate the role of strain in driving the observed multiple CDW orderings at the surface of $TbTe_3$, most likely by modifying local electron-phonon coupling within the surface layer. The interplay of lattice-strain anisotropy and electronic properties has been shown to be important in establishing the CDW states in the bulk of the $R$$Te_3$ compounds. Our measurements suggest the same is true at the surface. Using STM to simultaneously study local strain and local electronic properties has the potential to provide nanometer insight into this interplay.

ACKNOWLEDGMENTS

We thank Eric Hudson and Ming Yi for their comments on the paper. Samples used in this paper were grown at Stanford University, supported by the Department of Energy, Office of Basic Energy Sciences under Contract No. DE-AC02-76SF00515. This paper is also supported by Clark University (faculty development grants and university and physics department research student support).

L.F. and A.M.K. contributed equally to this work.

---

[1] K. C. Rahnejat, C. A. Howard, N. E. Shuttleworth, S. R. Schofield, K. Iwaya, C. F. Hirjibehedin, C. Renner, G. Aeppli, and M. Ellerby, Nat. Commun. **2**, 558 (2011).

[2] H. Mutka, Phys. Rev. B **28**, 2855 (1983).

[3] A. Briggs, P. Monceau, M. Nunez-Regueiro, M. Ribault, and J. Richard, J. Phys. (Paris) **42**, 1453 (1981).

[4] D. Andres, M. V. Kartsovnik, W. Biberacher, K. Neumaier, E. Schuberth, and H. Müller, Phys. Rev. B **72**, 174513 (2005).

[5] J. Chang, E. Blackburn, A. T. Holmes, N. B. Christensen, J. Larsen, J. Mesot, L. Ruixing, D. A. Bonn, W. N. Hardy, A. Watenphul, M. v. Zimmermann, E. M. Forgan, and S. M. Hayden, Nat. Phys. **8**, 871 (2012).

[6] L. E. Hayward, D. G. Hawthorn, R. G. Melko, and S. Sachdev, Science **343**, 1336 (2014).

[7] Y. Wang, D. F. Agterberg, and A. Chubukov, Phys. Rev. Lett. **114**, 197001 (2015).

[8] A. J. Achkar, F. He, R. Sutarto, C. McMahon, M. Zwiebler, M. Hucker, G. D. Gu, R. Liang, D. A. Bonn, W. N. Hardy, J. Geck, and D. G. Hawthorn, Nat. Mater. **15**, 616 (2016).

[9] W. D. Wise, M. C. Boyer, K. Chatterjee, T. Kondo, T. Takeuchi, H. Ikuta, Y. Wang, and E. W. Hudson, Nat. Phys. **4**, 696 (2008).

[10] T. Machida, Y. Fujisawa, M. Nagao, S. Demura, K. Deguchi, Y. Mizuguchi, Y. Takano, and H. Sakata, J. Phys. Soc. Jpn. **83**, 113701 (2014).

[11] G.-H. Gweon, J. D. Denlinger, J. W. Allen, R. Claessen, C. G. Olson, H. Hochst, J. Marcus, C. Schlenker, and L. F. Schneemeyer, J. Electron Spectrosc. Relat. Phenom. **117–118**, 481 (2001).

[12] J.-L. Mozos, P. Ordejón, and E. Canadell, Phys. Rev. B **65**, 233105 (2002).

[13] J. Schäfer, E. Rotenberg, S. D. Kevan, P. Blaha, R. Claessen, and R. E. Thorne, Phys. Rev. Lett. **87**, 196403 (2001).

[14] G. H. Gweon, J. W. Allen, J. A. Clack, Y. X. Zhang, D. M. Poirier, P. J. Benning, C. G. Olson, J. Marcus, and C. Schlenker, Phys. Rev. B **55**, R13353 (1997).

[15] M. D. Johannes, I. I. Mazin, and C. A. Howells, Phys. Rev. B **73**, 205102 (2006).

[16] M. D. Johannes and I. I. Mazin, Phys. Rev. B **77**, 165135 (2008).

[17] A. Soumyanarayanan, M. M. Yee, Y. He, J. van Wezel, D. J. Rahn, K. Rossnagel, E. W. Hudson, M. R. Norman, and J. E. Hoffman, Proc. Natl. Acad. Sci. USA **110**, 1623 (2013).

[18] C. J. Arguello, S. P. Chockalingam, E. P. Rosenthal, L. Zhao, C. Gutiérrez, J. H. Kang, W. C. Chung, R. M. Fernandes, S. Jia, A. J. Millis, R. J. Cava, and A. N. Pasupathy, Phys. Rev. B **89**, 235115 (2014).

[19] J. Dai, E. Calleja, J. Alldredge, X. Zhu, L. Li, W. Lu, Y. Sun, T. Wolf, H. Berger, and K. McElroy, Phys. Rev. B **89**, 165140 (2014).

[20] C. D. Malliakas and M. G. Kanatzidis, J. Am. Chem. Soc. **128**, 12612 (2006).

[21] C. Malliakas, S. J. L. Billinge, H. J. Kim, and M. G. Kanatzidis, J. Am. Chem. Soc. **127**, 6510 (2005).

[22] A. Sacchetti, C. L. Condron, S. N. Gvasaliya, F. Pfuner, M. Lavagnini, M. Baldini, M. F. Toney, M. Merlini, M. Hanfland, J. Mesot, J. H. Chu, I. R. Fisher, P. Postorino, and L. Degiorgi, Phys. Rev. B **79**, 201101 (2009).

[23] E. DiMasi, M. C. Aronson, J. F. Mansfield, B. Foran, and S. Lee, Phys. Rev. B **52**, 14516 (1995).

[24] N. Ru, C. L. Condron, G. Y. Margulis, K. Y. Shin, J.Laverock, S. B. Dugdale, M. F. Toney, and I. R. Fisher, Phys. Rev. B **77**, 035114 (2008).

[25] A. Banerjee, Y. Feng, D. M. Silevitch, J. Wang, J. C. Lang, H. H. Kuo, I. R. Fisher, and T. F. Rosenbaum, Phys. Rev. B **87**, 155131 (2013).

[26] R. G. Moore, V. Brouet, R. He, D. H. Lu, N. Ru, J. H. Chu, I. R. Fisher, and Z. X. Shen, Phys. Rev. B **81**, 073102 (2010).

[27] J. Laverock, S. B. Dugdale, Z. Major, M. A. Alam, N. Ru, I. R. Fisher, G. Santi, and E. Bruno, Phy. Rev. B **71**, 085114 (2005).

[28] H. Yao, J. A. Robertson, E.-A. Kim, and S. A. Kivelson, Phys. Rev. B **74**, 245126 (2006).

[29] M. Maschek, S. Rosenkranz, R. Heid, A. H. Said, P. Giraldo-Gallo, I. R. Fisher, and F. Weber, Phys. Rev. B **91**, 235146 (2015).

[30] H.-M. Eiter, M. Lavagnini, R. Hackl, E. A. Nowadnick, A. F. Kemper, T. P. Devereaux, J.-H. Chu, J. G. Analytis, I. R. Fisher, and L. Degiorgi, Proc. Natl. Acad. Sci. USA **110**, 64 (2013).

[31] R. G. Moore, W. S. Lee, P. S. Kirchman, Y. D. Chuang, A. F. Kemper, M. Trigo, L. Patthey, D. H. Lu, O. Krupin, M. Yi, D. A. Reis, D. Doering, P. Denes, W. F. Schlotter, J. J. Turner, G. Hays, P. Hering, T. Benson, J.-H. Chu, T. P. Devereaux, I. R. Fisher, Z. Hussain, and Z.-X. Shen, Phys. Rev. B **93**, 024304 (2016).

[32] N. Ru and I. R. Fisher, Phys. Rev. B **73**, 033101 (2006).

[33] A. Fang, N. Ru, I. R. Fisher, and A. Kapitulnik, Phys. Rev. Lett. **99**, 046401 (2007).

[34] A. Tomic, Z. Rak, J. P. Veazey, C. D. Malliakas, S. D. Mahanti, M. G. Kanatzidis, and S. H. Tessmer, Phys. Rev. B **79**, 085422 (2009).

[35] A. T. Tomic, Ph.D. thesis, Michigan State University, 2008.

[36] V. Brouet, W. L. Yang, X. J. Zhou, Z. Hussain, N. Ru, K. Y. Shin, I. R. Fisher, and Z. X. Shen, Phys. Rev. Lett. **93**, 126405 (2004).

[37] W. S. Lee, A. P. Sorini, M. Yi, Y. D. Chuang, B. Moritz, W. L. Yang, J.-H. Chu, H. H. Kuo, A. G. Cruz Gonzalez, I. R. Fisher, Z. Hussain, T. P. Devereaux, and Z. X. Shen, Phys. Rev. B **85**, 155142 (2012).

[38] G. Gruner, *Density Waves in Solids (Frontiers in Physics)* (Addison-Wesley Publishing Company, Reading, Massachusetts, 1994), Vol. 89, p. 259.

[39] H. Ando, T. Yokoya, K. Ishizaka, S. Tsuda, T. Kiss, S. Shin, T. Eguchi, M. Nohara, and H. Takagi, J. Phys.: Condens. Matter **17**, 4935 (2005).

[40] J. Schäfer, M. Sing, R. Claessen, E. Rotenberg, X. J. Zhou, R. E. Thorne, and S. D. Kevan, Phys. Rev. Lett. **91**, 066401 (2003).

[41] C. Brun, Z.-Z. Wang, and P. Monceau, Phys. Rev. B **80**, 045423 (2009).

[42] M. H. Whangbo, E. Canadell, and C. Schlenker, J. Am. Chem. Soc. **109**, 6308 (1987).

[43] D. Mou, A. Sapkota, H. H. Kung, V. Krapivin, Y. Wu, A. Kreyssig, X. Zhou, A. I. Goldman, G. Blumberg, R. Flint, and A. Kaminski, Phys. Rev. Lett. **116**, 196401 (2016).

[44] G. H. Gweon, S. K. Mo, J. W. Allen, C. R. Ast, H. Höchst, J. L. Sarrao, and Z. Fisk, Phys. Rev. B **72**, 035126 (2005).

[45] H. Fujisawa, H. Kumigashira, T. Takahashi, R. Kurita, and M. Koyano, Surface Rev. and Lett. **09**, 1041 (2002).

[46] P. Mallet, K. M. Zimmermann, P. Chevalier, J. Marcus, J. Y. Veuillen, and J. M. Gomez Rodriguez, Phys. Rev. B **60**, 2122 (1999).

[47] P. Mallet, H. Guyot, J. Y. Veuillen, and N. Motta, Phys. Rev. B **63**, 165428 (2001).

[48] V. Brouet, W. L. Yang, X. J. Zhou, Z. Hussain, R. G. Moore, R. He, D. H. Lu, Z. X. Shen, J. Laverock, S. B. Dugdale, N. Ru, and I. R. Fisher, Phys. Rev. B **77**, 235104 (2008).

[49] M. Saint-Paul, C. Guttin, P. Lejay, G. Remenyi, O. Leynaud, and P. Monceau, Solid State Commun. **233**, 24 (2016).

[50] B. Cordero, V. Gomez, A. E. Platero-Prats, M. Reves, J. Echeverria, E. Cremades, F. Barragan, and S. Alvarez, Dalton Trans. **2008**, 2832 (2008).

[51] K. Momma and F. Izumi, J. Appl. Crystallogr. **44**, 1272 (2011).